

Local structural changes in $\text{LiMn}_{1.5}\text{Ni}_{0.5}\text{O}_4$ spinel cathode material for lithium-ion batteries

Jatinkumar Rana ^{a,*}, Sven Glatthaar ^b, Holger Gesswein ^b, Neeraj Sharma ^c, Joachim R. Binder ^b, Roman Chernikov ^d, Gerhard Schumacher ^a, John Banhart ^{a,e}

^a Helmholtz-Zentrum Berlin für Materialien und Energie, Hahn-Meitner-Platz 1, 14109 Berlin, Germany

^b Institut für Angewandte Materialien, Karlsruher Institut für Technologie, Hermann-von-Helmholtz-Platz 1, 76344 Eggenstein-Leopoldshafen, Germany

^c School of Chemistry, University of New South Wales, Sydney, NSW 2052, Australia

^d Deutsches Elektronen-Synchrotron, Notkestrasse 85, 22607 Hamburg, Germany

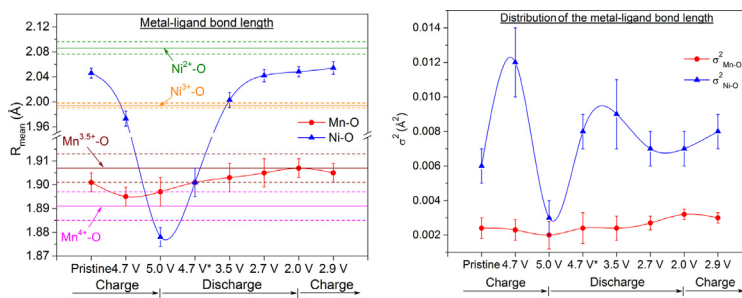
^e Technische Universität Berlin, Hardenbergstrasse 36, 10623 Berlin, Germany



HIGHLIGHTS

- Design of the electrochemical cell for in-operando structural characterization of electrode materials for lithium-ion batteries.
- Correlation between electrochemical and structural changes in $\text{Li}_x\text{Mn}_{1.5}\text{Ni}_{0.5}\text{O}_4$.
- Reversible cubic to tetragonal phase transition upon insertion/extraction of excess Li ($x > 1$) in $\text{Li}_x\text{Mn}_{1.5}\text{Ni}_{0.5}\text{O}_4$.

GRAPHICAL ABSTRACT



ARTICLE INFO

Article history:

Received 12 November 2013

Received in revised form

20 December 2013

Accepted 8 January 2014

Available online 18 January 2014

Keywords:

$\text{LiMn}_{1.5}\text{Ni}_{0.5}\text{O}_4$

Li-ion batteries

EXAFS

XANES

Structural changes

ABSTRACT

Local structural changes in $\text{LiMn}_{1.5}\text{Ni}_{0.5}\text{O}_4$ cathode material were investigated by X-ray absorption spectroscopy in-operando using a specially designed electrochemical cell. The average structure of the starting material determined by neutron powder diffraction confirmed partial ordering of Mn and Ni cations on the octahedral sites in the spinel structure. It is observed that the electrochemical activity of the material between 3.5 V and 5.0 V is largely attributed to a two-step $\text{Ni}^{2+}/\text{Ni}^{4+}$ redox reaction. However, a small fraction of Mn^{3+} present in the pristine material also participates in electrochemical processes via a $\text{Mn}^{3+}/\text{Mn}^{4+}$ redox reaction. The excess lithium inserted into the material during deep discharge of the cell down to 2.0 V causes a further reduction of Mn^{4+} to Mn^{3+} , while Ni remains electrochemically inactive. An increased proportion of Mn^{3+} in the material increases the distortion of MnO_6 octahedra by the Jahn-Teller effect, which locally reduces the crystal symmetry from cubic to tetragonal, giving rise to the formation of domains of a $\text{Li}_2\text{Mn}_2\text{O}_4$ -type tetragonal phase. The fraction of this tetragonal phase was found to be directly related to the excess lithium inserted into the material. Upon subsequent charging to 2.9 V, the tetragonal phase tends to revert back to the original cubic spinel phase. The observed decline in the electrochemical performance of the material when cycled between 2.0 V and 5.0 V may be attributed to repetitive structural changes associated with the cubic \leftrightarrow tetragonal phase transition.

© 2014 Elsevier B.V. All rights reserved.

* Corresponding author.

E-mail address: jatinkumar.rana@helmholtz-berlin.de (J. Rana).

1. Introduction

$\text{LiMn}_{1.5}\text{Ni}_{0.5}\text{O}_4$ constitutes an important class of cathode materials for rechargeable lithium-ion batteries. The higher operating voltage of the material (~ 5 V) and 3D diffusion of lithium ions in its spinel structure give rise to batteries with high energy density and high-rate capabilities. Depending on the synthesis conditions, $\text{LiMn}_{1.5}\text{Ni}_{0.5}\text{O}_4$ can exist in two different crystallographic modifications: a cation disordered face-centered cubic spinel with the space group $Fd\bar{3}m$ and its ordered variant where cation ordering on the octahedral sites lowers crystal symmetry to cubic primitive (space group $P4_332$) [1]. The substitution of Mn by Ni in $\text{LiMn}_{1.5}\text{Ni}_{0.5}\text{O}_4$ tends to stabilize the average valence of manganese ions at $4+$ and, thereby, improves the electrode performance by suppressing the dissolution of manganese in the electrolyte due to the disproportionation reaction [2,3] and Jahn-Teller distortion [4–7] during discharge. Powder X-ray diffraction has been widely used for characterizing cathode materials for lithium-ion batteries [6,8–13]. However, this technique provides information about average changes in the long-range structure of crystalline materials, while the electrochemical performance of cathode materials is largely governed by local structural modifications occurring in the vicinity of transition metal (TM) cations during battery cycling.

We investigate local structural changes in $\text{Li}_x\text{Mn}_{1.5}\text{Ni}_{0.5}\text{O}_4$ by X-ray absorption spectroscopy (XAS) with the aim to elucidate electrochemical processes upon inserting the excess lithium ($x > 1$) into the material. The element selectivity of XAS offers a unique opportunity to probe chemical, electronic and geometrical changes at and around individual types of absorbing atoms in the material. The near-edge region of the absorption spectra, called the X-ray Absorption Near Edge Structure (XANES), provides qualitative information about the average valence state of absorbing atoms, their local symmetry, electronic configuration etc., while the extended region, called the Extended X-ray Absorption Fine Structure (EXAFS), provides quantitative information about geometrical changes in the vicinity of absorbing atoms. There are several reports dealing with the XAS characterization of similar lithium manganese oxide spinels [14,15]. However, these reports largely focused on estimating changes in the valence of TM cations based on the observed chemical shifts in their absorption spectra, often known as the fingerprint approach, with little emphasis on quantifying geometrical changes occurring in the material as a result of electrochemical cycling. In the present study, we review the validity of such an empirical approach in determining the valence of absorbing atoms. Besides, structural modifications in the vicinity of Mn and Ni cations of the material are quantified by fitting a theoretical model to the EXAFS data at various states of charge and discharge.

2. Experimental

$\text{LiMn}_{1.5}\text{Ni}_{0.5}\text{O}_4$ was synthesized by the sol–gel method. Lithium acetate $\text{Li}(\text{CH}_3\text{COO}) \cdot 2\text{H}_2\text{O}$ (AlfaAesar), manganese acetate $\text{Mn}(\text{CH}_3\text{COO})_2 \cdot 4\text{H}_2\text{O}$ (Aldrich) and nickel acetate $\text{Ni}(\text{CH}_3\text{COO})_2 \cdot 4\text{H}_2\text{O}$ (Aldrich) were dissolved in distilled water under continuous stirring. The precursor solution was prepared by mixing these aqueous solutions of the acetates in stoichiometric ratios. Precursor powder was obtained by spray drying (Niro MOBILE MINORTM) the precursor solution under nitrogen atmosphere at 383 K. The precursor powder was then subjected to a two-step calcination process to form $\text{LiMn}_{1.5}\text{Ni}_{0.5}\text{O}_4$. In the first-step, the precursor powder was calcined at 773 K for 6 h under flowing dry air (flow rate 300 l h^{-1}) using a standard heating and cooling rate of 5 K min^{-1} . However, during pyrolysis between 553–623 K, a heating rate of 1 K min^{-1} was applied and oxygen was introduced. In the second-step, the powder

was further annealed at 1073 K for 12 h and then cooled down to room temperature at a rate of 1 K min^{-1} in order to minimize oxygen vacancies in the material. The crystal structure of the as-synthesized material was modeled by Rietveld analysis of neutron powder diffraction data using the software package GSAS/EXPGUI [16,17]. The data were collected at room temperature on the high-resolution neutron powder diffractometer, ECHIDNA [18], at the Open Pool Australian Light-water (OPAL) reactor facility using monochromatic neutrons of wavelength $1.6235(1) \text{ \AA}$.

Cathodes were prepared by mixing 90 wt. % active material, 5 wt. % carbon black (TIMCAL), and 5 wt. % of polyvinylidene difluoride (Arkema) as a binder. The resultant slurry was tape cast on an aluminum current collector using N-methyl-2-pyrrolidone as a solvent and left unpressed. After drying at 353 K for 12 h, a circular disc of 12 mm diameter was punched out of the slurry-coated aluminum current collector and constitutes the cathode of the cell. The cathode contained $\sim 14 \text{ mg cm}^{-2}$ of active material. A lithium metal anode was used as the counter electrode. A solution of 1 M LiPF_6 in 50 wt. % ethylene carbonate (EC) and 50 wt. % dimethyl carbonate (DMC) was used as the electrolyte (Merck LP30, water content: max. 20 ppm, HF content : max. 50 ppm). An electrolyte-impregnated glass fiber (Whatman GF/C) in addition to Celgard 2325 membrane was used as a separator. Fig. 1a and b show schematic and pictorial views of the electrochemical cell used in the present study. Our cell design is based on a coin cell geometry. The coin cell was assembled in a glove box. The cathode, anode and separators were placed inside a coin cell and the latter was placed inside the steel enclosure of the electrochemical cell as shown in Fig. 1a. The coin cell was provided with holes of 6 mm diameter on both sides which were sealed with the Kapton tape (not visible in the side view of the cell in Fig. 1a) to form hermetically sealed X-ray transmission windows. However, there are certain challenges associated with such an in-operando experiment such as corrosive reactions of the electrolyte with cell components and the oxidation of the lithium metal anode upon exposure to air due to an improper sealing of the X-ray transmission windows. With the present cell design, since the electrolyte was confined only to the inner part of the coin cell, the rest of the cell components are protected from corrosion. Also, once assembled in a glove box, the coin cell could be safely handled in air without any oxidation of the lithium metal anode. This allowed us to measure multiple cathode systems simply by replacing the coin cell containing the desired cathode system into the steel enclosure of the electrochemical cell at the beamline.

XAS data were recorded in the transmission mode at the Mn and Ni K-edges of the material at various states of charge and discharge. Measurements were carried out at beamline C1 of the Hamburger Synchrotron Radiation Laboratory (HASYLAB), Hamburg, Germany. The beamline is equipped with a Si (111) double crystal monochromator. Absolute energy calibration of the monochromator was carried out by measuring a reference foil of pure element simultaneously with the cell. Gas-filled ionization chambers were used to record the intensities of the incident beam and beams transmitted through the cell and the reference foil. Higher harmonics were rejected by detuning the monochromator such that the intensity of the incident beam on the sample was 65% of the maximum beam intensity. For comparison, several reference compounds such as Mn_2O_3 , MnO_2 -Pyrolusite, NiO and LiNiO_2 were also measured. Data were aligned, normalized and background subtracted as described elsewhere [19] using the software ATHENA of the package IFEFFIT [20]. The normalized EXAFS signal was transformed to k-space and multiplied by k^3 in order to compensate for damping of the signal at high k . The resultant k^3 -weighted $\chi(k)$ signal was then Fourier transformed and left uncorrected for a phase shift. A model function was generated by performing *ab initio* calculations using the code FEFF8.2 [21] and least-square

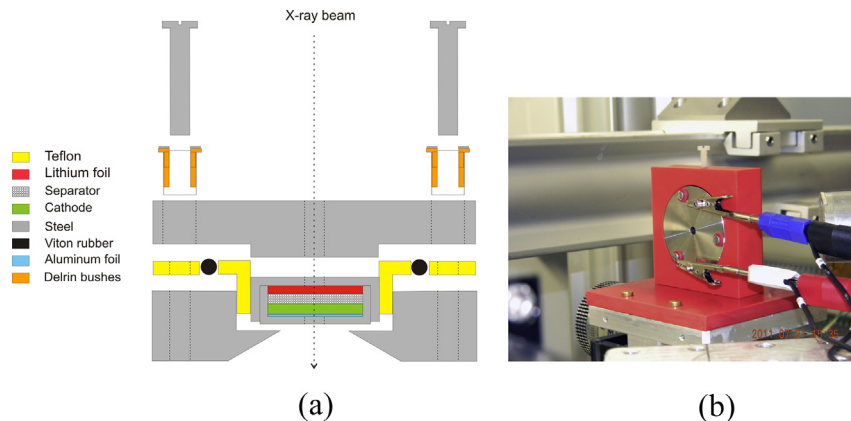


Fig. 1. (a) Schematic and (b) pictorial views of the electrochemical cell used in the present study.

fitted to the data using the software ARTEMIS of the package IFEFFIT [20]. The fitting parameters involved a single amplitude reduction factor S_0^2 and an overall energy parameter ΔE_0 for each data set. A fractional change in the bond length α_{fit} was refined for each coordination shell such that a change in the bond length ΔR was given by $\alpha_{\text{fit}} \times R_{\text{theory}}$. Additionally, each coordination shell, depending on the type of the backscattering atoms it contained and its mean distance from the central absorbing atom, was assigned a separate mean-squared relative displacement parameter σ^2 . The parameters for multiple scattering paths were constrained in terms of those of corresponding single scattering paths [22]. The statistical quality of an EXAFS fit was evaluated based on its R -factor.

3. Results

Fig. 2 illustrates the Rietveld refinement of neutron powder diffraction data of the as-synthesized material. Structural parameters obtained from Rietveld analysis are summarized in Table 1. The diffraction pattern exhibits superstructure peaks that can be indexed with the cubic primitive $P4_332$ space group. This is a clear indication of an ordering of Mn and Ni cations. However, Rietveld analysis reveals only partial ordering of these cations at the 4b and 12d octahedral sites (refer to Table 1). Such partial ordering of

cations which depends on synthesis conditions has also been reported previously [23]. It should be noted that the superstructure peaks corresponding to $P4_332$ space group were not observed in the XRD pattern of the material due to a small difference in the X-ray atomic form factors of Mn and Ni which gives rise to a poor scattering contrast. Besides, there is only partial ordering of these cations on the respective octahedral sites in the spinel structure which further contributes to the suppression of superstructure peaks in the XRD pattern. Based on the site occupation factors obtained by Rietveld analysis, the stoichiometry of the material can be estimated as $\text{LiMn}_{1.58}\text{Ni}_{0.48}\text{O}_4$ which agrees well in its overall chemical composition with $\text{Li}_{0.98}\text{Mn}_{1.53}\text{Ni}_{0.49}\text{O}_4$ as determined by Inductively Coupled Plasma/Optical Emission Spectroscopy (ICP/OES). A slight Ni deficiency in the composition derived from Rietveld analysis stems from the formation of a small amount of $\text{Li}_x\text{Ni}_{1-x}\text{O}$ -type impurity phase during synthesis (~ 2 wt.%).

The voltage profile and capacity of the cell obtained at various states of charge and discharge are presented in Fig. 3a and b. The cell was cycled at a rate of C/5 ($1\text{C} = 146.7 \text{ mA g}^{-1}$) which corresponds to a constant current (CC) of 29.3 mA g^{-1} . Once the cell reached a predetermined voltage, it was held at that constant voltage (CV) until the current flowing through the cell reduced to approximately zero (Fig. 3a). Only then the XAS spectra were recorded. It must be noted that the amount of active material used in the present study per unit area of the cathode ($\sim 14 \text{ mg cm}^{-2}$) was roughly three times higher than is normally used during laboratory electrochemical cycling. It was essential to employ such a high mass-loading of active material in order to record the data with a good signal-to-noise ratio at both the Mn and Ni absorption K-edges. However, in this situation, electrochemical reactions are

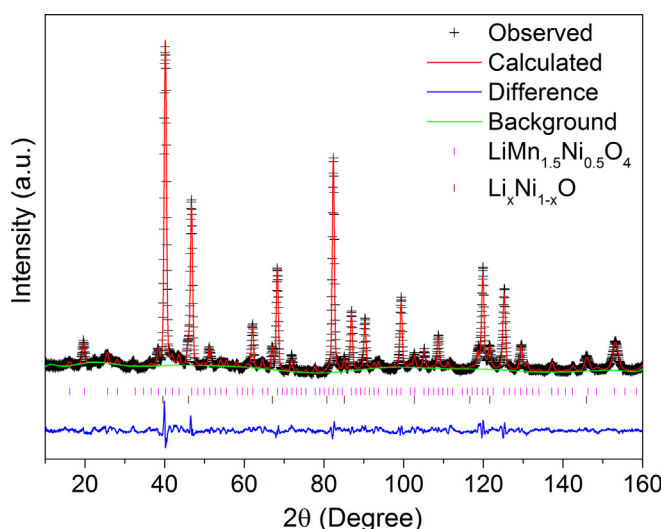


Fig. 2. Neutron powder diffraction pattern of the as-synthesized $\text{LiMn}_{1.5}\text{Ni}_{0.5}\text{O}_4$ along with the Rietveld fit.

Table 1

Rietveld refinement results for the as-synthesized $\text{LiMn}_{1.5}\text{Ni}_{0.5}\text{O}_4$. Space group $P4_332$, $a = b = c = 8.18072 \text{ \AA}$ and $\alpha = \beta = \gamma = 90^\circ$. The 8c site was assumed to be fully occupied by lithium ions, while 4b and 12d sites were assumed to be fully occupied by TM ions. Furthermore, the sum of the occupancies of TM ions at the 4b and 12d sites was assumed to be 1.

Atom	Wyckoff site	x	y	z	Occupancy	$U^a (\text{\AA}^2)$
Li(1)	8c	0.00272	0.00272	0.00272	1.0	0.01561
Ni(1)	4b	0.62500	0.62500	0.62500	0.486(5)	0.01215
Mn(1)	4b	0.62500	0.62500	0.62500	0.514(5)	0.01215
Mn(2)	12d	0.12500	0.38420	−0.13420	0.882(3)	0.01215
Ni(2)	12d	0.12500	0.38420	−0.13420	0.118(3)	0.01215
O(1)	8c	0.38759	0.38759	0.38759	1.0	0.01398
O(2)	24e	0.14089	−0.13860	0.13463	1.0	0.01398

^a Anisotropic displacement parameter.

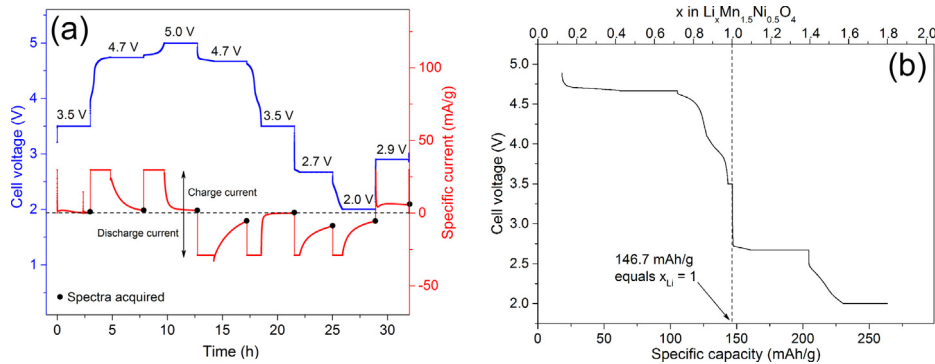


Fig. 3. Variation in the (a) cell-voltage and specific current and (b) specific capacity at various states of charge and discharge of $\text{LiMn}_{1.5}\text{Ni}_{0.5}\text{O}_4$ during an in-operando XAS measurements. The specific capacity in (b) was obtained by integrating the specific current in (a) over time.

seriously limited by the diffusion of lithium ions in the material. Thus, holding the cell at a CV step during such an in-operando study ensures that at any given potential all active material in the cathode has undergone electrochemical changes uniformly. As can be seen from Fig. 3b, a specific capacity of $\sim 128 \text{ mAh g}^{-1}$ delivered by the cell both during charge to 5 V and discharge to 3.5 V corresponds to the extraction/reinsertion of $x \approx 0.88$ Li from/into $\text{Li}_{(1-x)}\text{Mn}_{1.5}\text{Ni}_{0.5}\text{O}_4$. However, the excess lithium inserted into the material by further discharging the cell down to 2.0 V resulted into an additional capacity of $\sim 136 \text{ mAh g}^{-1}$. Fig. 4 illustrates the cycling performance of the material. When cycled between 3.5 V and 5.0 V, the material delivers a steady capacity of $\sim 125 \text{ mAh g}^{-1}$. However, there is a gradual loss in the capacity when the material is cycled between 2.0 V and 5.0 V.

3.1. XANES

Fig. 5a represents the XANES region at the Mn K-edge of $\text{LiMn}_{1.5}\text{Ni}_{0.5}\text{O}_4$ at various states of charge and discharge. The absorption K-edge is characterized by a variety of edge features such as an absorption threshold, the pre-edge region corresponding to the $1s \rightarrow 3d$ transition and a vertically rising main edge with a maximum corresponding to the $1s \rightarrow 4p$ transition [24]. A relative shift in the position of these edge features, called the chemical shift,

provides an empirical mean of estimating changes in the average valence state of absorbing atoms. In principle, with an increasing formal valence state of absorbing atoms, all these features should systematically shift to higher energy and vice versa [24–26]. However, since the outer p -orbitals are more sensitive to chemical changes, chemical shifts observed at the position of the $1s \rightarrow 4p$ peak are more pronounced [24,26]. As shown in Fig. 5a, the position of the $1s \rightarrow 4p$ peak at the Mn K-edge shifts to higher energy beyond that of the Mn^{4+} -containing reference compound as the cell is charged up to 5.0 V and it returns back to the original position during discharge to 3.5 V. As the cell is further discharged down to 2.0 V, this peak continues to shift to lower energy and upon subsequent charging to 2.9 V it reverses to higher energy again. Thus, there is a reversible shift in the position of this peak during charge and discharge. However, a consistent shift is not observed for other edge features, especially along the vertically rising main edge where spectra cross and no clear trend is seen.

Quite contrarily, chemical shifts at the Ni K-edge (Fig. 5b) appear less complex. In the pristine state, the position of the $1s \rightarrow 4p$ peak lies between those of Ni^{2+} and Ni^{3+} -containing reference compounds. As the cell is charged, this peak shifts to higher energy and remains beyond that of the Ni^{3+} reference compound at 5.0 V. During discharge, the peak shifts to lower energy and returns back to its original position at 2.7 V. However, there is no change in the position of this peak when the cell is further discharged down to 2.0 V and then charged to 2.9 V. The pre-edge region at the Mn K-edge (inset in Fig. 5a) is characterized by a splitting of the $1s \rightarrow 3d$ peak into t_{2g} and e_g peaks with the intensity of the e_g peak being notably higher than that of the t_{2g} peak. Furthermore, the intensity of these pre-edge peaks increases when the cell is charged and decreases when it is discharged. In contrast to this, the pre-edge region at the Ni K-edge (inset in Fig. 5b) is characterized by a weak $1s \rightarrow 3d$ peak. Consequently, changes in the intensity of this pre-edge peak during charge and discharge are not observable.

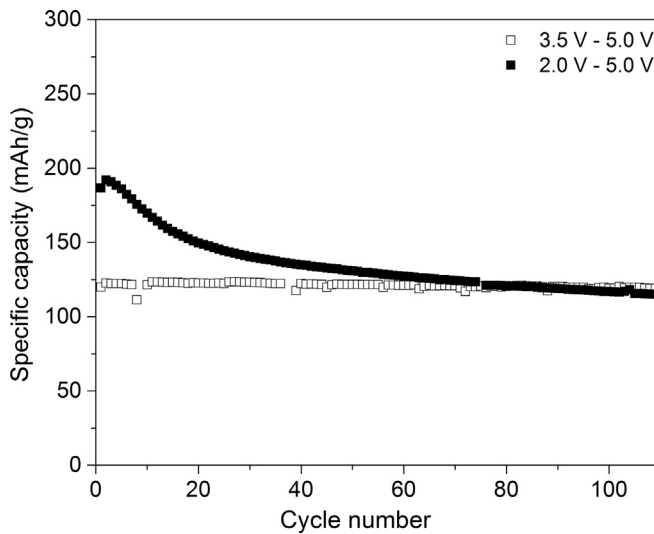


Fig. 4. Comparison of the electrochemical performance of $\text{LiMn}_{1.5}\text{Ni}_{0.5}\text{O}_4$ when cycled between 3.5 V–5.0 V and 2.0 V–5.0 V.

3.2. EXAFS

Fig. 6a represents the k^3 -weighted $\chi(k)$ signals at the Ni K-edge of $\text{LiMn}_{1.5}\text{Ni}_{0.5}\text{O}_4$. Qualitatively, there is a gradual change in the $\chi(k)$ signal as the cell is charged up to 5.0 V. However, the signal approximates that of the pristine state during discharge to 2.7 V. There are no significant changes in this signal when the cell is further discharged down to 2.0 V and then re-charged to 2.9 V. In the corresponding Fourier transforms in Fig. 6b, a peculiar variation in the amplitude of the 1st peak corresponding to the 1st shell of oxygen atoms around Ni (i.e. Ni–O1) is noteworthy. During charge,

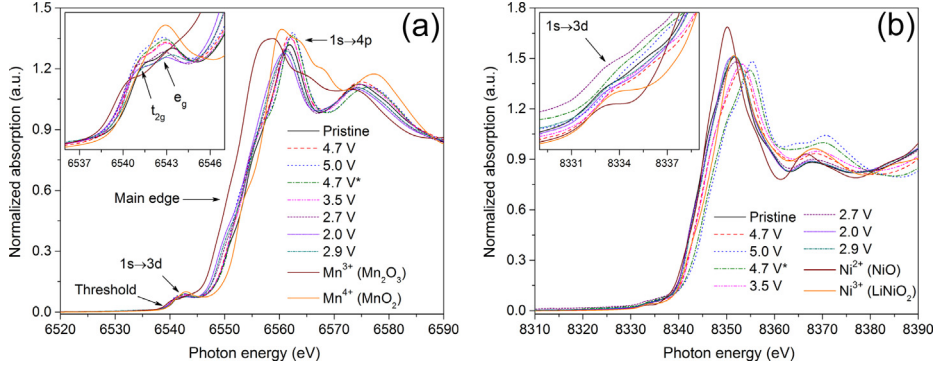


Fig. 5. Normalized absorption spectra at the (a) Mn and (b) Ni K-edges of $\text{LiMn}_{1.5}\text{Ni}_{0.5}\text{O}_4$ in various states of charge and discharge. The asterisk (*) represents the state measured during discharge.

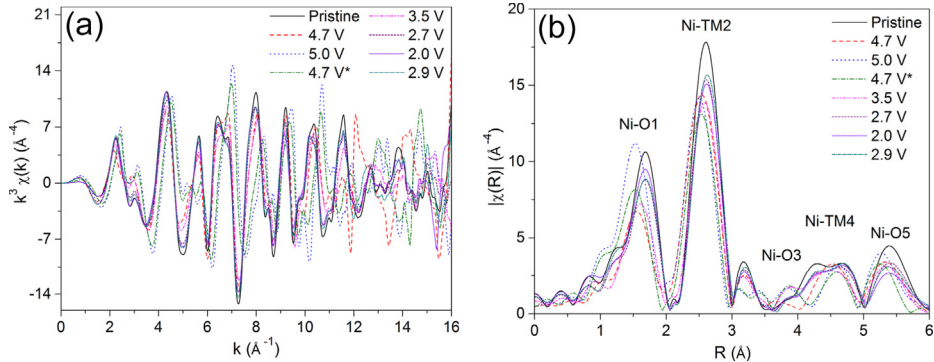


Fig. 6. (a) k^3 -weighted EXAFS signals $\chi(k)$ and (b) their Fourier transforms at the Ni K-edge of $\text{LiMn}_{1.5}\text{Ni}_{0.5}\text{O}_4$ in various states of charge and discharge. Notations: Ni–O1 corresponds to oxygen atoms in the 1st shell around Ni absorbers, Ni-TM2 corresponds to TM atoms in the 2nd shell around Ni absorbers and so on. Discrete data points are presented by lines for the sake of clarity. For raw data, see Fig. 8.

the amplitude of this peak first decreases at 4.7 V and then increases at 5.0 V. During discharge, the amplitude decreases until 3.5 V and then increases again when further discharging down to 2.0 V. Upon subsequent charging to 2.9 V, this amplitude begins to decrease again.

Fig. 7a shows the k^3 -weighted $\chi(k)$ signals at the Mn K-edge of $\text{LiMn}_{1.5}\text{Ni}_{0.5}\text{O}_4$, while their corresponding Fourier transforms are presented in Fig. 7b. As can be seen from Fig. 7a, measurements at the Mn K-edge were terminated at $k \sim 12 \text{\AA}^{-1}$ which corresponds to photon energy of approximately 7100 eV due to the presence of iron impurities in the lithium metal anode and, consequently, the onset of the Fe K-edge at 7112 eV. Nevertheless, a systematic change

in the amplitude of the Fourier transform peaks in Fig. 7b is clearly visible. The amplitude of these peaks gradually increases as the cell is charged up to 5.0 V and then decreases during discharge down to 2.0 V. Upon subsequent charging to 2.9 V, the amplitude of these peaks begins to increase again.

Partial ordering of Mn and Ni cations at the 4b and 12d sites (Table 1) in the spinel structure gives rise to two different local environments around these cations (Tables S1 and S2 in the Supporting Information (SI)). Therefore, fitting the EXAFS data either at the Mn or Ni K-edge requires averaging and weighting these two local environments based on the fractional occupancy of cations occupying these crystallographic positions by factors :

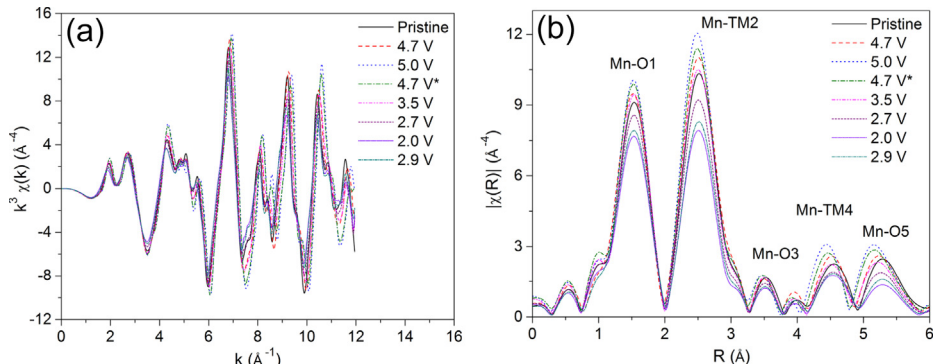


Fig. 7. (a) k^3 -Weighted EXAFS signals $\chi(k)$ and (b) their Fourier transforms at the Mn K-edge of $\text{LiMn}_{1.5}\text{Ni}_{0.5}\text{O}_4$ in various states of charge and discharge. Notations: Mn–O1 corresponds to oxygen atoms in the 1st shell around Mn absorbers, Mn-TM2 corresponds to TM atoms in the 2nd shell around Mn absorbers and so on. Discrete data points are presented by lines for the sake of clarity. For raw data, see Fig. 9.

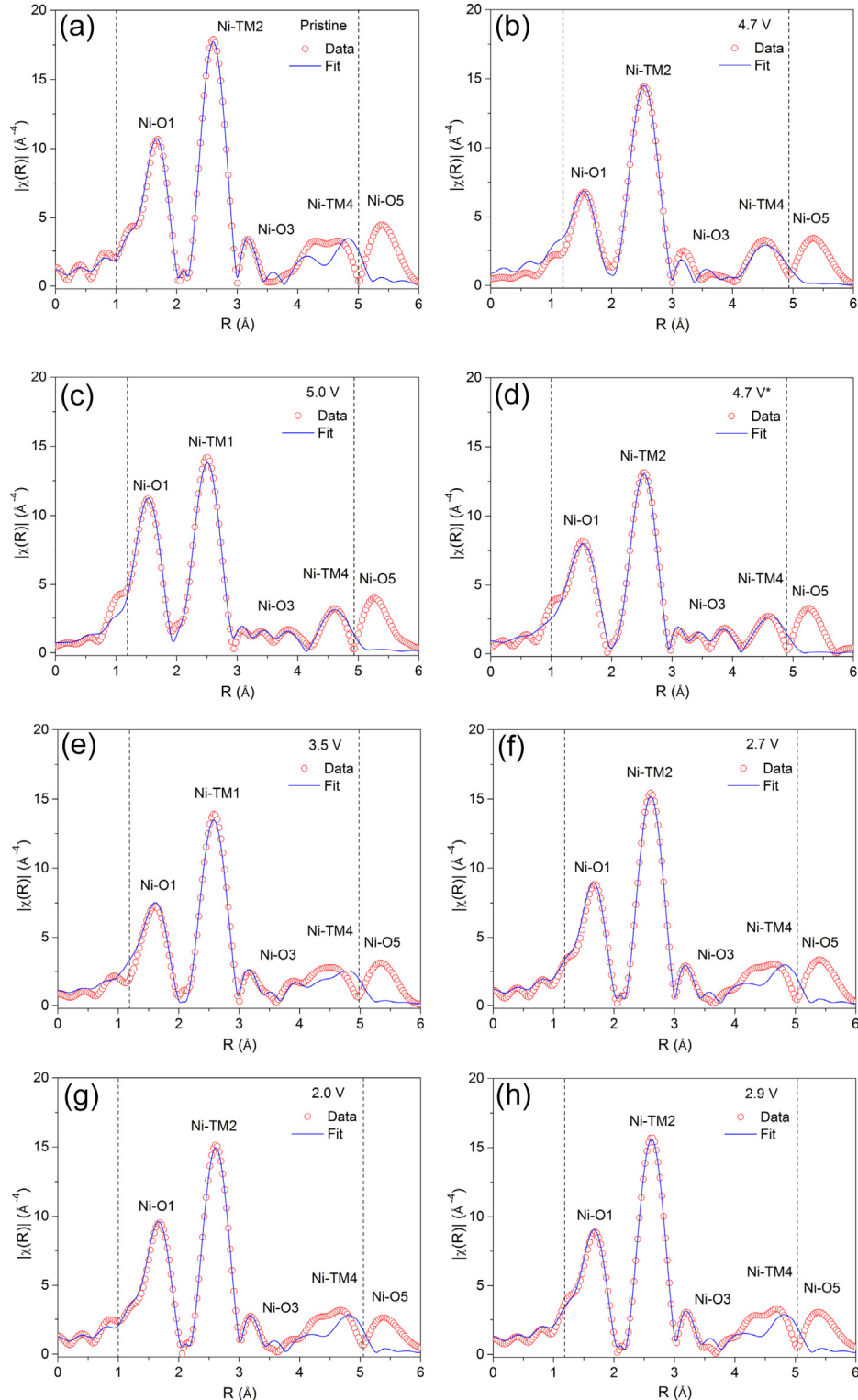


Fig. 8. EXAFS fits to the data measured at the Ni K-edge of $\text{LiMn}_{1.5}\text{Ni}_{0.5}\text{O}_4$ in various states of charge and discharge. Dotted lines indicate the fitting range.

$$W_{\text{Mn}(12d)} = f_{\text{Mn}} \times \frac{\gamma_{\text{Mn}(12d)}}{\gamma_{\text{Mn}(4b)} + \gamma_{\text{Mn}(12d)}}. \quad (1)$$

$$W_{\text{Mn}(4b)} = f_{\text{Mn}} \times \frac{\gamma_{\text{Mn}(4b)}}{\gamma_{\text{Mn}(4b)} + \gamma_{\text{Mn}(12d)}}. \quad (2)$$

$$W_{\text{Ni}(12d)} = f_{\text{Ni}} \times \frac{\gamma_{\text{Ni}(12d)}}{\gamma_{\text{Ni}(4b)} + \gamma_{\text{Ni}(12d)}}. \quad (3)$$

$$W_{\text{Ni}(4b)} = f_{\text{Ni}} \times \frac{\gamma_{\text{Ni}(4b)}}{\gamma_{\text{Ni}(4b)} + \gamma_{\text{Ni}(12d)}}. \quad (4)$$

Here, $f_{\text{Mn}} = 0.75$ and $f_{\text{Ni}} = 0.25$ are the atomic fractions of Mn and Ni cations in the material assuming the nominal stoichiometry $\text{LiMn}_{1.5}\text{Ni}_{0.5}\text{O}_4$. $\gamma_{\text{Mn}(12d)}$ and $\gamma_{\text{Ni}(12d)}$ represent the occupancies of Mn and Ni cations at the 12d site. Similarly, $\gamma_{\text{Mn}(4b)}$ and $\gamma_{\text{Ni}(4b)}$ represent the occupancies of Mn and Ni cations at the 4b site. The *FEFF* calculations corresponding to Mn absorbers at the 12d and 4b sites were weighted by the factors $W_{\text{Mn}(12d)}$ (Equation (1)) and $W_{\text{Mn}(4b)}$ (Equation (2)). In an identical manner, the *FEFF* calculations

corresponding to Ni absorbers at the 12d and 4b sites were weighted by the factors $W_{\text{Ni}(12d)}$ (Equation (3)) and $W_{\text{Ni}(4b)}$ (Equation (4)). As shown in **Tables S1 and S2 in the SI**, the 3rd shell of O atoms is split into shorter and longer bond lengths. At the Mn K-edge, these two bond lengths were constrained under the same ΔR and σ^2 parameters, since assigning them separate fitting parameters did not significantly improve the statistical quality of a fit. However, at the Ni K-edge, the best fit to the data was achieved by

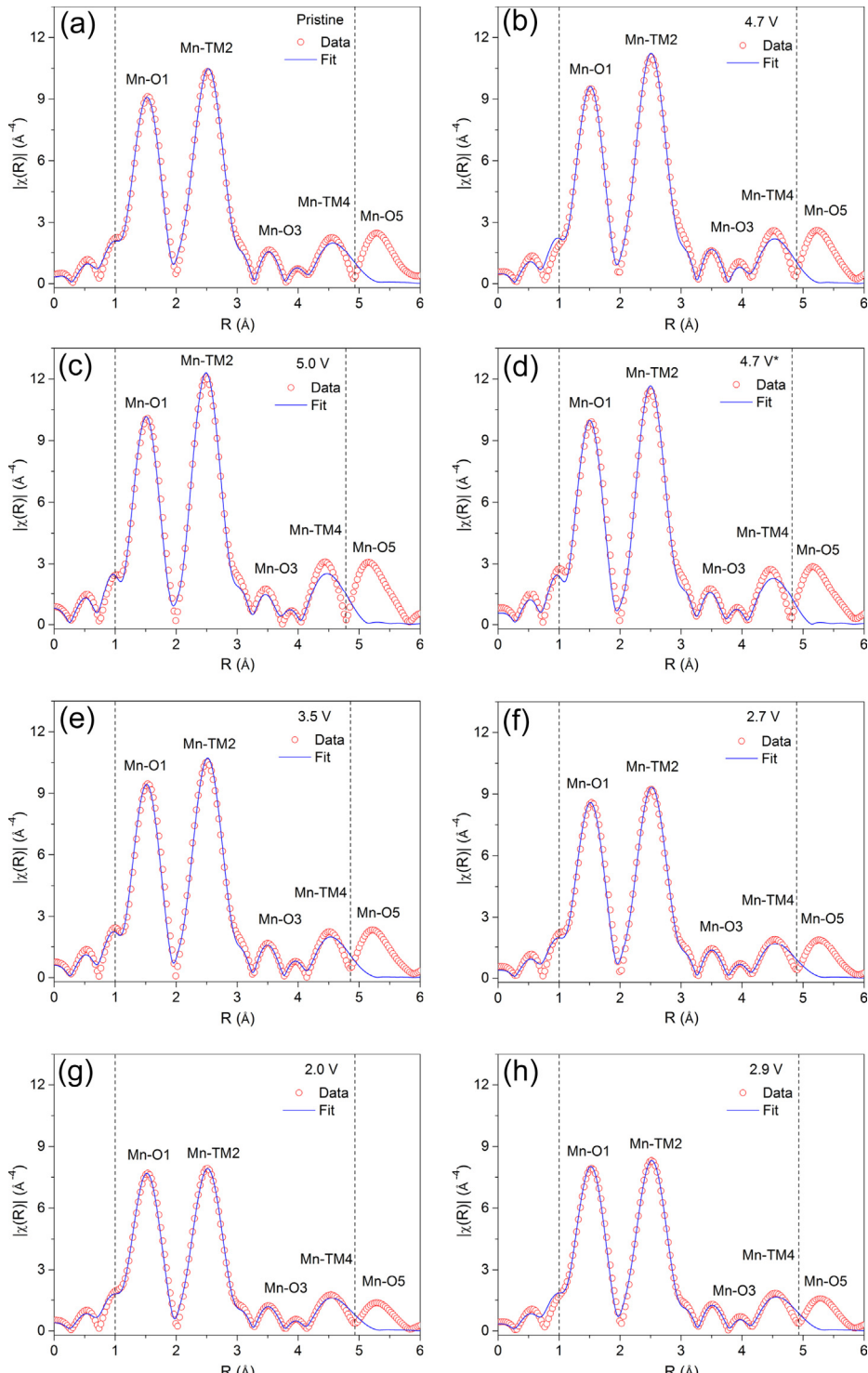


Fig. 9. EXAFS fits to the data measured at the Mn K-edge of $\text{LiMn}_{1.5}\text{Ni}_{0.5}\text{O}_4$ in various states of charge and discharge.

assigning separate ΔR and σ^2 parameters to these bond lengths. It has been claimed that at higher degrees of lithiation, the cubic spinel structure of LiMn_2O_4 undergoes a Jahn-Teller distortion, giving rise to the formation of a $\text{Li}_2\text{Mn}_2\text{O}_4$ -type tetragonal phase [4,5,13]. A deep discharge of the cell below 3.5 V corresponds to the insertion of excess Li ($x > 1$) into $\text{Li}_x\text{Mn}_{1.5}\text{Ni}_{0.5}\text{O}_4$ (Fig. 3b). Therefore, EXAFS data for all states below 3.5 V were explained by an additional tetragonal phase $\text{Li}_2\text{Mn}_2\text{O}_4$ (space group $I4_1/\text{amd}$) [4]. The fraction of this phase was refined to 0.08(8), 0.14(6) and 0.12(6) at 2.7 V, 2.0 V and 2.9 V, respectively. EXAFS fits to the data measured at the Ni and Mn K-edges are shown in Figs. 8 and 9, respectively. The refined values of bond lengths and their distribution (σ^2) for various coordination shells around Ni and Mn cations are reported in Tables S3–S6 in the SI. The statistical EXAFS fit parameters at the Ni and Mn K-edges are reported in Table S7 in the SI. Good agreement between the data and theory for all states can be seen by their R-factors that are ≤ 0.02 .

Fig. 10 shows the variation in the average bond length of various coordination shells around Mn and Ni cations. For all shells, the bond length decreases during charge and increases during discharge. Fig. 10a illustrates changes in the average metal-ligand bond length around Mn and Ni cations. For comparison, the average metal-ligand bond lengths of various reference compounds of Mn and Ni are also presented. The average $\text{Mn}^{3.5+}$ –O (LiMn_2O_4) and Mn^{4+} –O (MnO_2) bond lengths were obtained from the literature [27], while those of Ni^{2+} –O and Ni^{3+} –O are obtained by fitting the EXAFS data of NiO (Ni^{2+}) and LiNiO_2 (Ni^{3+}) reference compounds (Fig. S1 and Table S8 in the SI). In the pristine state, the average Ni–O bond length lies between those of Ni^{2+} –O and Ni^{3+} –O. It decreases during charge and attains a minimum value at 5.0 V. During discharge, this bond length increases and becomes similar

to that of the pristine state at 2.7 V. However, upon further discharge of the cell down to 2.0 V and subsequent charging to 2.9 V, this bond length remains unchanged. On the other hand, the average Mn–O bond length in the pristine state lies between those of $\text{Mn}^{3.5+}$ –O and Mn^{4+} –O. It decreases slightly as the cell is charged to 5.0 V and then increases again upon discharge to 3.5 V. However, upon deep discharge of the cell down to 2.0 V, the average Mn–O bond length continues to increase and upon subsequent charging to 2.9 V it begins to decrease again. Also, for the 1st and 2nd shells (Fig. 10a and b), changes in the bond length around Ni cations are larger than around Mn cations. However, these changes are not distinguishable for the 3rd and 4th shells (Fig. 10c and d).

The σ^2 parameter represents the distribution of the backscattering atoms around their mean position measured with respect to the central absorbing atom. This distribution can be either caused by thermal vibrations of atoms (thermal disorder) or by static displacements of atoms (static disorder) [28,29]. Since all XAS data reported in the present study are recorded at the same temperature (i.e. room temperature) and on the same cell, a systematic variation in the σ^2 parameter corresponding to any coordination shell represents a systematic variation in the distribution of the bond length corresponding to that particular shell resulting from electrochemical processes, while neglecting thermal disorder. As shown in Fig. 11, there is a slight decrease in the distribution width of the average Mn–O bond length as the cell is charged to 5.0 V and an increase when it is discharged to 3.5 V and further down to 2.0 V. This width begins to decrease upon subsequent charging to 2.9 V. However, these subtle changes in the distribution of the average Mn–O bond length are accompanied by large statistical uncertainties. On the other hand, the changes in the distribution of the

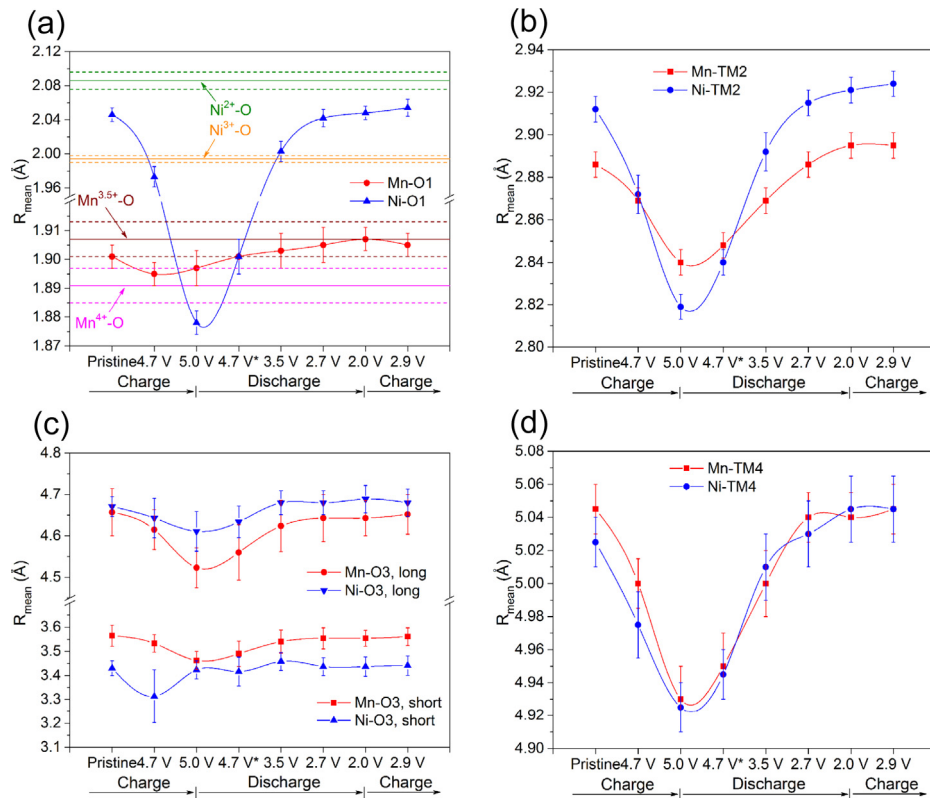


Fig. 10. Changes in the average bond length of various coordination shells around Mn and Ni cations of $\text{LiMn}_{1.5}\text{Ni}_{0.5}\text{O}_4$ at various states of charge and discharge. The solid lines in (a) indicate the average metal-ligand bond length obtained by fitting the EXAFS data of Ni^{2+} , Ni^{3+} , $\text{Mn}^{3.5+}$ and Mn^{4+} -containing reference compounds and dotted lines represent uncertainties of the fitted value. Use of notations as in Figs. 6–9. Lines are guide to eyes.

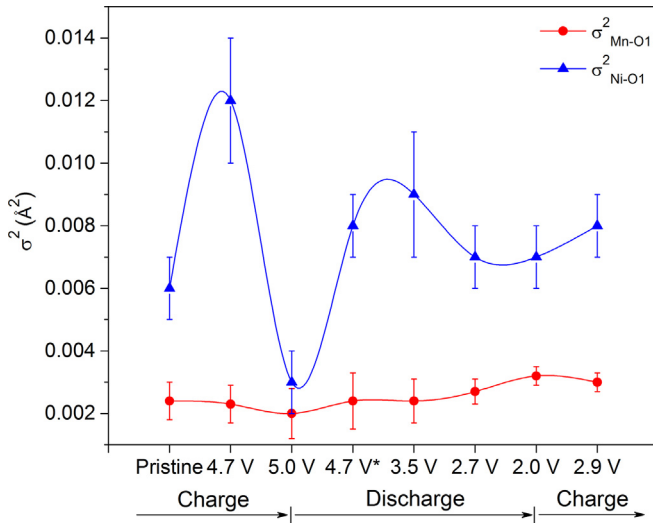


Fig. 11. Variation in the distribution of the metal-ligand bond length around Mn and Ni cations of $\text{LiMn}_{1.5}\text{Ni}_{0.5}\text{O}_4$ in various states of charge and discharge. Lines are guide to eyes.

average Ni–O bond length are quite large and follow a peculiar trend. In the pristine state, the width of this distribution is higher than that of the average Mn–O bond length. During charge, it first increases at 4.7 V and then decreases at 5.0 V. During discharge, this distribution again increases until 3.5 V and then decreases and becomes similar to that of the pristine state at 2.7 V. Upon further discharging the cell down to 2.0 V, this distribution remains unchanged from that at 2.7 V, but it begins to increase upon subsequent charging to 2.9 V.

4. Discussion

4.1. XANES

Chemical shifts in the absorption spectra are widely used as empirical means of estimating changes in the valence of absorbing atoms [24,25,30–37]. However, besides valence, these chemical shifts are also affected by type, symmetry and number of nearest neighbors, character of bond etc. [24]. The extent to which each of these features affects the observed chemical shifts varies not only from one material to another, but also from one absorbing atom type to another in the same material. This can be rationalized by examining the XANES region at the Mn and Ni K-edges of $\text{LiMn}_{1.5}\text{Ni}_{0.5}\text{O}_4$ in Fig. 5. The observed shift in the position of the $1s \rightarrow 4p$ peak at the Mn K-edge to higher energy during charge suggesting the oxidation of Mn^{4+} ions is not consistent with the fact that Mn^{4+} , when octahedrally coordinated as in $\text{LiMn}_{1.5}\text{Ni}_{0.5}\text{O}_4$, cannot be further oxidized [38]. Moreover, the cross-over of spectra along the main edge further complicates the interpretation of these chemical shifts. In this situation, an estimation of Mn valence depends on the choice of the reference point. A similar problem was encountered in the past by other groups [35–37]. Quite contrarily, chemical shifts at the Ni K-edge clearly suggest the oxidation and reduction of Ni cations during charge and discharge, respectively. Thus, a fingerprint approach based on the observed chemical shifts yields different conclusions at the Mn and Ni K-edges and, hence, is ambiguous. Contrary to this, the average metal-ligand bond length determined by fitting the EXAFS data provides conclusive evidence about changes in the valence of absorbing atoms since this bond length primarily depends on the ionic radius of the absorbing atom, which in turn depends on its valence state. From this aspect, any

oxidation or reduction of TM ions would result in a corresponding decrease or increase in their average metal-ligand bond length, respectively. Therefore, the observed chemical shifts at the Mn and Ni K-edges will be discussed in the context of changes in the average metal-ligand bond length around these cations.

The observed splitting of Mn 3d orbitals into t_{2g} and e_g orbitals can be attributed to the crystal field of surrounding oxygen ligands [26,27,32]. The notably higher intensity of the e_g peak compared to the t_{2g} peak suggests that ejected photoelectrons occupy one of the high-lying e_g orbitals rather than the low-lying t_{2g} orbitals which describes $\text{LiMn}_{1.5}\text{Ni}_{0.5}\text{O}_4$ as a high-spin compound. The pre-edge peaks at the Mn K-edge are more pronounced than at the Ni K-edge which can be attributed to the relative occupancy of metal d -orbitals. If the average valence states of Mn and Ni cations in the pristine material are assumed to be 4+ and 2+, respectively, based on the nominal stoichiometry $\text{LiMn}_{1.5}\text{Ni}_{0.5}\text{O}_4$ of the material, then Mn^{4+} with an orbital electronic configuration $[\text{Ar}]3d^3$ exhibits less occupied d -orbitals and, consequently, higher transition probabilities than Ni^{2+} having an $[\text{Ar}]3d^8$ configuration.

4.2. EXAFS

Best fits to the EXAFS data at the Ni and Mn K-edges by the partially ordered cubic spinel structure (space group $P4_32$) complement the Rietveld refinement results and confirm partial ordering of Ni and Mn cations in $\text{LiMn}_{1.5}\text{Ni}_{0.5}\text{O}_4$ as has also been reported previously [1,11]. In the pristine state, the average Ni–O (metal-ligand) bond length of the 1st shell lies between those of Ni^{2+} –O and Ni^{3+} –O (Fig. 10a), indicating the presence of Ni^{3+} along with Ni^{2+} in the starting material. It should be noted that the resolution in R-space (δ_R) is limited by the available data range in k-space ($\Delta k = k_{\max} - k_{\min}$) such that $\delta_R = \pi/2\Delta k$. For $\Delta k \sim 8 \text{ \AA}^{-1}$ at the Ni K-edge (Table S7 in SI), δ_R is limited to $\sim 0.2 \text{ \AA}$. This implies that two bond lengths separated by less than 0.2 \AA cannot be resolved as separate peaks in the Fourier transform. The average Ni^{2+} –O bond length of $2.086(10) \text{ \AA}$ differs from $1.994(4) \text{ \AA}$ of Ni^{3+} –O by $\sim 0.1 \text{ \AA}$ (refer to Table S8 in SI) and, hence, these two bond lengths cannot be resolved as separate Fourier transform peaks in R-space. Rather, the information concerning the coexistence of Ni^{2+} and Ni^{3+} in the material can be captured from the σ^2 parameter corresponding to the average Ni–O bond length of the 1st shell. From this aspect, a larger distribution of the average Ni–O bond length in the pristine material (Fig. 11) confirms the coexistence of Ni^{3+} and Ni^{2+} . However, the presence of Ni^{3+} in the pristine material accounts for an excess positive charge which must be compensated by the presence of a small amount of Mn^{3+} . This is consistent with the average Mn–O bond length of the 1st shell lying between those of $\text{Mn}^{3.5+}$ –O and Mn^{4+} –O (Fig. 10a), confirming the presence of a small amount of Mn^{3+} along with Mn^{4+} in the pristine state, as has also been reported previously [39,40].

As shown in Fig. 10a, a gradual reduction in the average Ni–O bond length during charge suggests oxidation of $\text{Ni}^{2+}/\text{Ni}^{3+}$ to Ni^{4+} . This is consistent with the fact that the average Ni–O bond length of $1.878(4) \text{ \AA}$ at 5.0 V is very similar to that observed for the Ni^{4+} -containing compound [41]. However, the distribution of the average Ni–O bond length ($\sigma^2_{\text{Ni}-\text{O}1}$) first widens at 4.7 V and then narrows at 5.0 V (Fig. 11), suggesting that the oxidation of Ni^{2+} to Ni^{4+} occurs in two steps, i.e. oxidation of Ni^{2+} to Ni^{3+} and that of Ni^{3+} to Ni^{4+} . Since the different ionic radii of Ni^{2+} , Ni^{3+} and Ni^{4+} would result in varying Ni–O bond lengths, the wider distribution of the average Ni–O bond length during charge at 4.7 V confirms the coexistence of multivalent Ni ions in the material. During charge, the fraction of Ni^{2+} decreases, while that of Ni^{4+} increases continuously through Ni^{3+} until 5.0 V where all Ni^{2+} has been oxidized to Ni^{4+} and uniform Ni^{4+} –O bond lengths are observed.

Consequently, the distribution of the average Ni–O bond length narrows at 5.0 V. The observed changes in the EXAFS signals at the Ni K-edge as the cell is charged up to 5.0 V (Figs. 6a and 8a–c) suggest changes in the local atomic arrangement around Ni absorbers and may be correlated to the proposed migration of Ni⁴⁺ ions to the vacant lithium sites during lithium extraction [10]. However, attempts to quantify the fraction of Ni migrated to the vacant lithium sites for the charged states were unsuccessful. Upon discharging the cell to 4.7 V, the EXAFS signal remains similar to that observed at 5.0 V (Fig. 8c and d). However, at 3.5 V, the signal approximates that of the pristine state (Fig. 8a and e). This may be attributed to the reverse migration of Ni from the lithium sites back to the TM sites during lithium reinsertion. The average Ni–O bond length (Fig. 10a) and its distribution (Fig. 11) increase during discharge which once again confirms the two-step reduction of Ni⁴⁺ to Ni²⁺ and, in turn, explains a wider distribution of the average Ni–O bond length during discharge.

At 2.7 V, both the average Ni–O bond length and its distribution become similar to those in the pristine state, indicating the reduction of Ni⁴⁺ back to a mixture of Ni²⁺/Ni³⁺ as observed in the starting material. Upon further discharging the cell to 2.0 V, the EXAFS signal remains unchanged from that observed at 2.7 V (Fig. 8f and g). Similarly, there are no changes in the average Ni–O bond length and its distribution (Figs. 10a and 11). These results suggest that Ni does not participate in the electrochemical processes below 2.7 V and that the local atomic arrangement around Ni remains unchanged upon excess lithiation. Upon subsequently charging the cell to 2.9 V, the distribution of the average Ni–O bond length begins to increase, indicating the onset of the oxidation of Ni²⁺/Ni³⁺ ions during lithium extraction. The observed peculiar change in the amplitude of the 1st peak corresponding to the oxygen atoms in the 1st shell around Ni absorbers in Fig. 6b can now be correlated to a varying distribution of the average Ni–O bond length as a result of the stepwise oxidation and/or reduction of Ni cations during charge and/or discharge. The observed chemical shifts at the Ni K-edge (Fig. 5b) are in agreement with the variation in the average Ni–O bond length. Both these results confirm the Ni²⁺/Ni⁴⁺ redox reaction.

At the Mn K-edge, there are no significant changes in the EXAFS signals when the cell is charged up to 5.0 V (Fig. 9a–c) which suggests that unlike Ni⁴⁺ ions, Mn⁴⁺ ions remain confined to the octahedral TM sites and do not migrate to the vacant lithium sites during lithium extraction. A subtle decrease in the average Mn–O bond length when the cell is charged up to 5.0 V may be attributed to the oxidation of a small fraction of Mn³⁺, present in the pristine material, to Mn⁴⁺. Similarly, an increase in this bond length upon discharge of the cell to 3.5 V may be correlated to the reduction of a small fraction of Mn⁴⁺ back to Mn³⁺. This is consistent with the observed changes in the intensity of the pre-edge peaks at the Mn K-edge (inset in Fig. 5a). Previously, changes in the intensity of the pre-edge peak have been observed to correlate with changes in the average metal-ligand bond length, i.e. the higher the intensity of the pre-edge peak, the shorter is the average metal-ligand bond length and vice versa [24,27]. Thus, the observed increase and decrease in the intensity of the pre-edge peaks at the Mn K-edge can be correlated to a systematic decrease and increase in the average Mn–O bond length, respectively, which in turn confirms a small electrochemical activity from the Mn³⁺/Mn⁴⁺ redox reaction when the material is cycled between 3.5 V and 5.0 V. This is also consistent with the observed increase or decrease in the amplitude of the EXAFS signals at the Mn K-edge during charge and discharge, respectively (Fig. 7b), which can be correlated to a varying distribution of the average Mn–O bond length as a result of varying proportions of Mn³⁺ and Mn⁴⁺ ions in the material. Thus, changes in the average metal-ligand bond length and the width of its

distribution provide direct evidence for the redox activity of each of the TM ions present in the material. A large change in the average Ni–O bond length than in the average Mn–O bond length of the 1st shell during charge and discharge of the cell clearly suggests a large contribution of Ni cations to the overall electrochemical activity of the material. However, changes in the bond length beyond the 1st shell may not be directly correlated to the redox activity of the TM ions. For instance, changes in the average Mn–TM bond length of the 2nd shell (Fig. 10b) are larger than in the average Mn–O bond length of the 1st shell since both Mn absorbers and the backscattering TM ions undergo changes in their ionic radii as a result of their oxidation/reduction during charge/discharge. Consequently, larger changes in the Mn–TM bond length of the 2nd shell are observed than in the Mn–O bond length of the 1st shell where only a small fraction of Mn³⁺ undergoes a Mn³⁺/Mn⁴⁺ redox reaction. However, for the 3rd and 4th shells (Fig. 10c and d), changes in the bond length around Ni and Mn cations remain indistinguishable which describes XAS as a local probe, extremely sensitive to changes in the vicinity of absorbing atoms.

However, upon deep discharge of the cell down to 2.0 V, both the average Mn–O bond length and the width of its distribution continue to increase from those at 3.5 V (Figs. 10a and 11). These results suggest that the excess Li ($x_{\text{Li}} > 1$) inserted into $\text{Li}_x\text{Mn}_{1.5}\text{Ni}_{0.5}\text{O}_4$ is charge-compensated by further reduction of Mn⁴⁺ to Mn³⁺. An increased proportion of Mn³⁺ in the material causes an increased distortion of MnO₆ octahedra by the Jahn-Teller effect [6,7,42]. The observed reduction in the amplitude of the EXAFS signals at the Mn K-edge below 3.5 V (Fig. 7b) can now be attributed to this static disorder introduced into the material upon excess lithiation. The distortion of MnO₆ octahedra locally reduces the crystal symmetry from cubic to tetragonal, giving rise to the formation of domains of a $\text{Li}_2\text{Mn}_2\text{O}_4$ -type tetragonal phase [4,5,13,43]. At 2.7 V, the fraction of this tetragonal phase was refined to 0.08(8), indicating the onset of the Jahn-Teller effect. However, at 2.0 V, the fraction of this phase was increased to 0.14(6) which suggests that structural distortion is directly related to the excess lithium inserted into the material. Upon subsequent charging of the cell to 2.9 V, both the average Mn–O bond length and its distribution begin to decrease, indicating the onset of the oxidation of Mn³⁺ ions during lithium extraction. Furthermore, the fraction of the tetragonal phase was slightly decreased to 0.12(6) at 2.9 V, suggesting a reversible nature of the cubic to tetragonal phase transition during charge as has also been reported elsewhere [13]. The cubic to tetragonal phase transition that occurs at higher degrees of lithiation reportedly involves a large change in lattice parameters [4]. The deteriorating electrochemical performance of the material when cycled between 2.0 V and 5.0 V (Fig. 4) may be attributed to such large, repetitive structural changes which may develop high intraparticle stresses and eventually lead to cracking of particles. This may result in a loss of contacts between particles and the current collector and, consequently, a loss of capacity upon cycling.

5. Conclusions

In the present work, local structural modifications in the vicinity of Mn and Ni cations of $\text{LiMn}_{1.5}\text{Ni}_{0.5}\text{O}_4$ cathode material were investigated at various states of charge and discharge. Rietveld analysis of neutron powder diffraction data of the as-synthesized material confirmed partial ordering of Mn and Ni cations on octahedral sites of the spinel structure. It is observed that an empirical approach involving an estimation of the average valence state of absorbing atoms solely based on the observed chemical shifts in the absorption spectra can be highly subject to personal bias and often misleading. However, changes in the average metal-ligand bond length and its distribution in combination with the observed edge

features can provide more reliable information about changes in the valence of absorbing atoms. Based on these criteria, the presence of a small amount of Ni³⁺ along with Ni²⁺ and, consequently, a small amount of Mn³⁺ along with Mn⁴⁺ were detected in the pristine material. Both, the variation in the average Ni–O bond length and its distribution suggest that the electrochemical activity of the material when cycled between 3.5 V and 5.0 V is largely attributed to a two-step Ni²⁺/Ni⁴⁺ redox reaction. However, a small amount of Mn³⁺ present in the pristine material also participates in electrochemical processes via a Mn³⁺/Mn⁴⁺ redox reaction. During lithium extraction, Mn⁴⁺ ions remain confined to the octahedral TM sites. However, there are indications of a possible migration of Ni⁴⁺ ions from the TM sites to the vacant lithium sites during Li extraction and back to the TM sites during lithium reinsertion. The excess lithium inserted into the material by deep discharge of the cell down to 2.0 V causes further reduction of Mn⁴⁺ to Mn³⁺, while Ni remains electrochemically inert. An increased proportion of Mn³⁺ in the material increases the distortion of MnO₆ octahedra by the Jahn-Teller effect, giving rise to the formation of domains of a Li₂Mn₂O₄-type tetragonal phase by locally reducing the crystal symmetry from cubic to tetragonal. Upon subsequent charging to 2.9 V, the tetragonal phase appears to revert back to the original cubic spinel. The deteriorating electrochemical performance of the material when cycled between 2.0 V and 5.0 V may be attributed to repetitive structural changes associated with the cubic \leftrightarrow tetragonal phase transition that occurs in the material each time the cell is charged and discharged across 3.5 V.

Acknowledgments

The authors acknowledge financial support from the Europäischer Fonds für regionale Entwicklung (EFRE) under the project BATMAT (No. 200720132/35).

Appendix A. Supplementary data

Supplementary data related to this article can be found at <http://dx.doi.org/10.1016/j.jpowsour.2014.01.037>

References

- [1] Y. Idemoto, H. Narai, N. Koura, *J. Power Sources* 119–121 (2003) 125–129.
- [2] D. Jang, Y. Shin, S. Oh, *J. Electrochem. Soc.* 143 (1996) 2204–2211.
- [3] Y. Xia, Y. Zhou, M. Yoshio, *J. Electrochem. Soc.* 144 (1997) 2593–2600.
- [4] M. Thackeray, W. David, P. Bruce, J. Goodenough, *Mater. Res. Bull.* 18 (1983) 461–472.
- [5] T. Ohzuku, M. Kitagawa, T. Hirai, *J. Electrochem. Soc.* 137 (1990) 769–775.
- [6] R. Gummow, A. de Kock, M. Thackeray, *Solid State Ionics* 69 (1994) 59–67.
- [7] M. Thackeray, Y. Shao-Horn, A. Kahaian, K. Kepler, E. Skinner, J. Vaughan, S. Hackney, *Electrochim. Solid-State Lett.* 1 (1998) 7–9.
- [8] M. Thackeray, A. de Kock, M. Rossouw, D. Liles, R. Bittihn, D. Hoge, *J. Electrochem. Soc.* 139 (1992) 363–366.
- [9] G. Pistoia, G. Wang, C. Wang, *Solid State Ionics* 58 (1992) 285–292.
- [10] J.-H. Kim, S.-T. Myung, C. Yoon, S. Kang, Y.-K. Sun, *Chem. Mater.* 16 (2004) 906–914.
- [11] Y. Idemoto, H. Sekine, K. Ui, N. Koura, *Solid State Ionics* 176 (2005) 299–306.
- [12] R. Alcantara, M. Jaraba, P. Lavela, J. Lloris, C. Perez Vicente, J. Tirado, *J. Electrochem. Soc.* 152 (2005) A13–A18.
- [13] K. Rhodes, R. Meisner, Y. Kim, N. Dudney, D. Claus, *J. Electrochem. Soc.* 158 (2011) A890–A897.
- [14] Y. Shiraiishi, I. Nakai, T. Tsubata, T. Himeda, F. Nishikawa, *J. Solid State Chem.* 133 (1997) 587–590.
- [15] Y. Terada, K. Yasaka, F. Nishikawa, T. Konishi, M. Yoshio, I. Nakai, *J. Solid State Chem.* 156 (2001) 286–291.
- [16] A. Larson, R. Von Dreele, Los Alamos Natl. Lab. Rep. LAUR 86-748, 2004, 1–224.
- [17] B. Toby, *J. Appl. Crystallogr.* 34 (2001) 210–213.
- [18] K.-D. Liss, B. Hunter, M. Hagen, T. Noakes, S. Kennedy, *Phys. B Condens. Matter* 385–386 (2006) 1010–1012.
- [19] S. Kelly, D. Hesterberg, B. Ravel, in: *Methods of Soil Analysis, Part 5 – Mineralogical Methods*, vol. 5, Soil Science Society of America, Madison, WI, USA, 2008, pp. 387–463.
- [20] B. Ravel, M. Newville, *J. Synchrotron Radiat.* 12 (2005) 537–541.
- [21] A. Ankudinov, B. Ravel, J. Rehr, S. Conradson, *Phys. Rev. B* 58 (1998) 7565–7576.
- [22] S. Calvin, Ph.D. thesis, The City University of New York, 2001.
- [23] A. Bhaskar, N. Bramnik, A. Senyshyn, H. Fuess, H. Ehrenberg, *J. Electrochem. Soc.* 157 (2010) A689–A695.
- [24] J. Wong, F. Lytle, R. Messmer, D. Maylotte, *Phys. Rev. B* 30 (1984) 5596–5610.
- [25] V. Sapre, C. Mandé, *J. Phys. C. Solid State Phys.* 5 (1972) 793–797.
- [26] O. Haas, A. Deb, E. Cairns, A. Wokaun, *J. Electrochem. Soc.* 152 (2005) A191–A196.
- [27] J. Rana, M. Stan, R. Kloepsch, J. Li, G. Schumacher, E. Welter, I. Zizak, J. Banhart, M. Winter, *Adv. Energy Mater.* (2013), <http://dx.doi.org/10.1002/aenm.201300998>. Accepted.
- [28] D. Sayers, E. Stern, F. Lytle, *Phys. Rev. Lett.* 27 (1971) 1204–1207.
- [29] J. Rehr, R. Albers, *Rev. Mod. Phys.* 72 (2000) 621–654.
- [30] C. Johnson, A. Kropf, *Electrochim. Acta* 47 (2002) 3187–3194.
- [31] C. Johnson, J.-S. Kim, A. Kropf, A. Kahaian, J. Vaughan, M. Thackeray, *J. Power Sources* 119–121 (2003) 139–144.
- [32] A. Deb, U. Bergmann, E. Cairns, S. Cramer, *J. Synchrotron Radiat.* 11 (2004) 497–504.
- [33] A. Deb, U. Bergmann, E. Cairns, S. Cramer, *J. Phys. Chem. B* 108 (2004) 7046–7051.
- [34] A. Deb, U. Bergmann, S. Cramer, E. Cairns, *J. Electrochem. Soc.* 154 (2007) A534–A541.
- [35] D. Yu, K. Yanagida, Y. Kato, H. Nakamura, *J. Electrochem. Soc.* 156 (2009) A417–A424.
- [36] D. Yu, K. Yanagida, *J. Electrochem. Soc.* 158 (2011) A1015–A1022.
- [37] A. Ito, Y. Sato, T. Sanada, M. Hatano, H. Horie, Y. Ohsawa, *J. Power Sources* 196 (2011) 6828–6834.
- [38] J. Saint, M. Doeff, J. Reed, *J. Power Sources* 172 (2007) 189–197.
- [39] Q. Zhong, A. Bonakdarpour, M. Zhang, Y. Gao, J. Dahn, *J. Electrochem. Soc.* 144 (1997) 205–213.
- [40] Z. Moorhead-Resenberg, D. Shin, K. Chemelewski, J. Goodenough, A. Manthiram, *Appl. Phys. Lett.* 100 (2012) 2139091–2139095.
- [41] T. Capehart, D. Corrigan, R. Conell, K. Pandya, R. Hoffman, *Appl. Phys. Lett.* 58 (1991) 865–867.
- [42] M. Thackeray, *J. Electrochem. Soc.* 142 (1995) 2558–2563.
- [43] M. Whittingham, *Chem. Rev.* 104 (2004) 4271–4301.